scientific reports

OPEN

Investigating orbital angular momentum modes in multimode interference (MMI) waveguides and revealing their mode conversion property

Afsoun Soltani[1], S. Faezeh Mousavi[2,3], Zaker Hossein Firouzeh[1✉], Abolghasem Zeidaabadi Nezhad[1] & Rahman Nouroozi[4]

In this work, the propagation of OAM modes in multimode interference (MMI) waveguides, as the basic elements in many integrated optical devices, is studied to utilize their benefits in integrated OAM applications. OAM modes shape the OAM-maintaining image at the specific length of an MMI waveguide. As the most effective parameters on the properties of the generated image, waveguide's width (W), topological charge (ℓ) and waist radius (WR) of the input OAM modes are investigated. Power overlap integral (POI) is used to evaluate the quality of images. The investigations show that the calculated POI is enhanced by increasing in WR of the input mode (from 86.91% for WR = 1.5 μm to 98.92% for WR = 3.5 μm; where W = 15 μm and $\ell = \pm 1$). Furthermore, the increase in the waveguide's width leads to decrease the quality of the self-imaged mode (from 98.90% for W = 15 μm to 85.15% for W = 50 μm; where WR = 3 μm and $\ell = \pm 1$). It is also demonstrated that mode conversion between even order of OAM modes with opposite topological charges can occur at OAM-maintaining length of the MMI waveguides, which is the most outstanding achievement of this survey for optical communication systems.

Pioneered by Allen in 1992[1], light beams with the phase dependence of $e^{i\ell\phi}$ carry OAM, independent of the polarization state, where ϕ is the azimuthal angle, and ℓ indicates the topological charge ($\ell = \pm 1, \pm 2, \ldots$). Topological charge represents the number of twists the light does in one wavelength. In order to process OAM modes, exploiting functionalities such as generation, transmission, and conversion are necessary. To date, generation and manipulation of OAM modes have been developed using several approaches including the spatial light modulators[2–4], spiral phase plates[5], q-plates[6,7], and diffractive phase holograms[8]. For the special case of OAM mode conversion, which is among the interested functionalities in this paper, using cylindrical lenses[1,9,10] and fiber gratings[11–15] have been widely reported to realize OAM convertors. For instance, as a seminal reported work, a suspended combination of two cylindrical lenses has been used to transform a Laguerre-Gaussian mode of OAM $-\ell\hbar$ per photon into one with $+\ell\hbar$ per photon[1], which has been shown the mechanical torque generation using the maximum transformation of OAM. Furthermore, the study of angular momentum interconversion with the aid of optical elements such as the hollow metallic cone, the solid dielectric cone and the metallic wedge has been represented[16].

Compared to the mentioned approaches, which suffer from drawbacks such as the complexity of optical alignment[12] and the necessity of precise control of parameters[17], the integrated implementations have been attracted due to the significant advantages in reliability, miniaturization and scalability[18]. There are two approaches for generating and manipulating OAM beams using photonic integrated circuits (PICs): out-of-plane and in-plane[19]. The out-of-plane method involves employing PIC elements or integrated light sources to induce scattered field formation, resulting in the desired OAM modes. Microring resonators[20,21], circular phase array emitters[22–24], and subwavelength gratings[25–28] are the different structural designs for out-of-plane generation

[1]Department of Electrical and Computer Engineering, Isfahan University of Technology, Isfahan 8415683111, Iran. [2]Department of Physics, University of Trieste, 34127 Trieste, Italy. [3]CNR-INO, National Institute of Optics, 34149 Trieste, Italy. [4]Department of Physics, Institute for Advanced Studies in Basic Sciences, Zanjan 45195-1159, Iran. ✉email: zhfirouzeh@iut.ac.ir

1

of OAM modes. In order to achieve sophisticated OAM functionalities on photonic chips, in-plane approach, which entails on-chip OAM beam generation or its controlled injection into the chip plane, is crucial[19]. The most common design structures used for in-plain OAM applications are rectangular waveguides. The computational and theoretical investigation into the prospect of OAM modes transmission over dielectric rectangular waveguides has been reported by Lyubopytov et al.[29]. Furthermore, an on-chip integrated structure including silicon waveguides and couplers has been presented, which can produce OAM modes with $\ell = \pm 1$[30]. A three-layer waveguide structure with the functions of the chirality conversion and the torque generation has also been proposed[31]. The presented convertor converts incident angular momentum into the opposite one. Additionally, an electro-optically active lithium niobate on insulator photonic wire configuration has been presented for manipulation of modes encoded in OAM-SAM states[32]. Moreover, a rectangular waveguide with a single trench has been designed to generate OAM modes with $\ell = \pm 1$[33]. In addition, the integrated rectangular platforms have been represented to generate OAM beam only on the longitudinal component of the electric field which made the application of proposed platforms complicated[34–36]. Additionally, the investigation of spin and orbital angular momentum of optical fields in a silicon channel waveguide has been proposed based on the superposition of two quasi-TE modes which are limited to the first order of OAM modes[37]. In another recent work, the design approach to a grating coupler for in-plane generation and propagation of quasi-TE vortex modes with azimuthal order of $\ell = \pm 1$ within PICs has been suggested[38].

In addition to the mentioned approaches, MMI structures, as a novel and actually neglected choice for integrated OAM applications, can be introduced which have many interesting features, such as their compact size, low sensitivity to fabrication parameters, and ease of fabrication[39]. In the last few years, MMI structures, based on the interference between the modes of a multimode waveguide, have widely been used in both one and two dimensions as the basic element in many integrated optical devices such as optical beam splitters[40–42], mode convertors[43], couplers[44], wavelength-division (de)multiplexers[45], and switches[46]. In one dimensional (1D) MMI devices the waveguide is single mode in the transverse dimension and multimode in the other dimension, whereas in two dimensional (2D) devices, MMI waveguides are multimode in both horizontal and vertical directions[47]. In order to carry the power by higher order modes with 2D field distributions, 2D MMI devices are required. From this point of view, 2D MMI structures can be utilized for OAM modes transmission. The use of 2D MMI structures for OAM modes, was first introduced by describing the self-imaging property of OAM modes in MMI waveguides[48], which means the input field profile can be reproduced in single or multiple images at periodic intervals along the propagation direction. 2D MMI waveguides for manipulation of beams carrying OAM has also been utilized to design an OAM mode convertor[49]. However, these structures still have many unknown potentials in using OAM modes which can make them an attractive and practical part of many circuits.

Accordingly, in this work, the propagation of OAM modes in 2D square cross-sectional MMI waveguides is investigated. OAM modes form the OAM-maintaining image at the specific length of an MMI waveguide. The properties of the OAM-maintaining image are studied by considering three main parameters including the width of the waveguide, the waist radius (WR) of the OAM mode and its topological charge. It is also represented theoretically, and confirmed by simulation results that OAM modes with odd and even values of charge have different behavior in MMI waveguides. For odd order of OAM modes, the generated images at the OAM-maintaining length of an MMI waveguide have the same topological charge as the input, whereas the even order ones are reversed ($\ell \rightarrow -\ell$). In addition to the topological charge, the propagation of OAM modes in MMI waveguides are affected by the width of MMI waveguide and WR of the input mode. These parameters are chosen in the ranges of 15–50 μm, and 1.5–3.5 μm, respectively for the investigation purposes of this paper. The properties and quality of the images along waveguides influenced by the referred parameters are discussed for OAM modes with odd and even values of ℓ, separately.

Theory

As mentioned in Introduction, 2D MMI waveguides support multiple modes in both horizontal and vertical directions. The analysis of these structures can be performed by extending the guided mode propagation analysis of 1D MMI structures to the 2D case. The guided modes of a 2D MMI waveguide (Fig. 1) with W_x lateral width and W_y vertical width in X and Y directions, respectively, have the form of the following equation[50]:

$$\psi_{uv}(x, y) = \psi_u(x)\psi_v(y) = \sin\left(\frac{\pi(u+1)}{W_x}x\right)\sin\left(\frac{\pi(v+1)}{W_y}y\right), \qquad (1)$$

where $u, v = 1, 2, 3, \ldots$ are the mode orders in X and Y directions, respectively. The corresponding longitudinal propagation constants are satisfied as:

$$\beta_{uv}^2 = k^2 n_g^2 - \left(\frac{\pi(u+1)}{W_x}\right)^2 - \left(\frac{\pi(v+1)}{W_y}\right)^2, \qquad (2)$$

where $k = 2\pi/\lambda_0$ indicates the wave number, λ_0 is the working wavelength in vacuum, and n_g represents the refractive index of the multimode waveguide. Neglecting the reflected field as well as the power coupled to the radiative modes, the incident field of $\Psi(x, y, 0)$ can be expressed as a superposition of the infinite numbers of guided modes as:

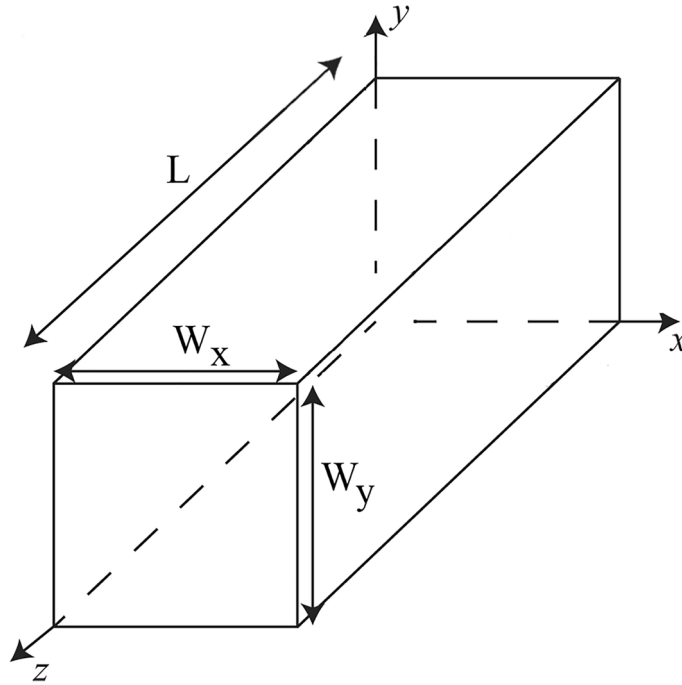$$\Psi(x, y, 0) = \sum_{u=0}\sum_{v=0} C_{uv}\psi_{uv}(x, y), \qquad (3)$$

where,

Fig. 1. Schematic diagram of a 2D MMI waveguide with W_x lateral width and W_y vertical width in X and Y directions, respectively.

$$C_{uv} = \frac{4}{W_x W_y} \int_0^{W_x} \int_0^{W_y} \Psi(x,y,0) \psi_{uv}(x,y) \, dx dy. \tag{4}$$

After propagating a distance L in the waveguide, the field profile $\Psi(x,y,L)$ can be expressed as:

$$\Psi(x,y,L) = \sum_{u=0} \sum_{v=0} \Psi(x,y,0) e^{j(\omega t - \beta_{uv} L)}, \tag{5}$$

Taking the fundamental mode out of the summation and using the paraxial approximation for the propagation constant in Eq. (2), the field profile can be written as:

$$\Psi(x,y,L) = e^{j(\omega t - \beta_{00} L)} \sum_{u=0} \sum_{v=0} \Psi(x,y,0) \times exp\left[j\frac{u(u+2)}{3L_{\pi x}}\pi L + j\frac{v(v+2)}{3L_{\pi y}}\pi L\right], \tag{6}$$

where $L_{\pi x}$ and $L_{\pi y}$ are the coupling lengths between the two lowest order modes in X and Y directions, respectively, as:

$$L_{\pi x} = \frac{\pi}{\beta_{00} - \beta_{10}} = \frac{4 n_g W_{xeff}^2}{3\lambda_0}, \tag{7}$$

$$L_{\pi y} = \frac{\pi}{\beta_{00} - \beta_{01}} = \frac{4 n_g W_{yeff}^2}{3\lambda_0}. \tag{8}$$

In these equations W_{xeff} and W_{yeff} denote the effective waveguide thicknesses, the former in X and the later in Y directions, as:

$$W_{xeff} = W_x + \frac{\lambda_0}{\pi \sqrt{n_g^2 - n_c^2}}, \tag{9}$$

$$W_{yeff} = W_y + \frac{\lambda_0}{\pi \sqrt{n_g^2 - n_c^2}}. \tag{10}$$

with n_c the cladding refractive index[51].

In multimode waveguides, an input field profile can be reproduced in single or multiple images at the periodic intervals along the propagation distance of the waveguide, according to the self-imaging property. In Eq. (6), the distance L to produce self-imaging can be expressed as[39]:

$$L = \left(\frac{S_x}{N}\right) 3L_{\pi x} = \left(\frac{S_y}{M}\right) 3L_{\pi y}. \tag{11}$$

where N and M are the positive integers without common divisors with the positive integers S_x and S_y, which are the positional numbers in X and Y directions, respectively. For simplicity, in the following discussion, $S_x = S_y = 1$, which is also a common practice for the shortest device length. In a square cross-sectional MMI waveguide ($W_x = W_y = W$, $L_{\pi x} = L_{\pi y} = L_c$, and $N = M$), if N is an even number ($N = 2K$, where K is an integer), the number of images at the length $L = 3L_c/N$ can be decreased. It is worth noting that odd values of K result K self-images for both symmetric and anti-symmetric inputs[48]. Therefore, as the OAM modes always have the anti-symmetric field components, $K = 1$ leads to produce only one image at the shortest length $3L_c/2$ of a 2D square cross-sectional MMI waveguide.

Results

In order to consider the self-imaging phenomenon of OAM modes in MMI waveguides, the mode propagation inside these waveguides is simulated using beam propagation method (BPM) by the commercially available simulation software package OptiBPM 13.1. All the simulations assume a silicon waveguide ($n_g = 3.45$) surrounded by silica ($n_c = 1.45$) at the working wavelength $\lambda_0 = 1550$ nm. The detailed consideration of this phenomenon is performed by studying three main parameters. The first one, which is related to the physical structure of the MMI waveguide, is the waveguide's width. Two other parameters associated with the properties of OAM modes, are WR and the order of the mode's topological charge.

Width

Width of the MMI waveguide directly specifies the required waveguide's length to generate the OAM-maintaining image. The considered widths in this study are in a range of 15–50 µm. Table 1 summarizes the calculated OAM-maintaining lengths for the waveguides with the mentioned widths. The results confirms that the wider waveguides need the longer length to produce OAM images.

WR

In order to investigate the effect of WR, the OAM modes with WR in a range of 1.5–3.5 µm are propagated along the waveguides with the considered widths in Table 1.

As a performance criterion, the power overlap integral (POI) between the input mode (E1) and the output generated image (E2) is calculated as:

$$POI = \frac{\left| \int_S E_1(x,y) E_2^*(x,y)\, dxdy \right|^2}{\int_S \left| E_1(x,y) \right|^2 dxdy \cdot \int_S \left| E_2(x,y) \right|^2 dxdy}. \tag{12}$$

The results are shown in Table 2 for the calculated POI (%) between the input first order of OAM modes with $\ell = \pm 1$ and the output produced image at OAM-maintaining length of the considered waveguides. They imply

Waveguide's width (µm)	15	20	25	30	35	40	50
OAM-maintaining length (µm) = 3Lc/2	1023	1809	2817	4049	5502	7179	11,199

Table 1. The calculated OAM-maintaining lengths for considered waveguides with widths in a range of 15–50 µm.

Waveguide's width (µm)	WR (µm)				
	1.5	2	2.5	3	3.5
15	86.91	94.75	97.88	98.90	98.92
20	71.75	89.65	95.58	97.84	98.82
25	56.36	81.13	93.79	95.83	97.72
30	51.44	73.50	87.76	95.40	96.70
35	41.54	68.32	87.17	93.20	96.64
40	34.78	64.40	84.12	91.12	94.91
50	25.03	49.98	72.32	85.18	91.66

Table 2. The calculated POI (%) between the input OAM modes with $\ell = \pm 1$ and the output produced image at OAM-maintaining length of the considered waveguides in Table 1.

that for each waveguide's width, the calculated POI increases with increasing WR of the input mode. In addition, for wider waveguides, a larger input mode's WR leads to a higher value of POI. These deductions can be clearly inferred from Figs. 2 and 3, which show the normalized power distributions and phase patterns of the input (top rows) first order OAM modes with WR = 2 μm (a), WR = 2.5 μm (b), and WR = 3 μm (c) and the output (bottom rows) generated self-images for MMI waveguides with 15 μm and 20 μm width, respectively.

Topological charge

The third considered parameter is the topological charge of OAM modes. In General, any order of OAM mode field can be indicated as the superposition of odd and even mode fields as[48]:

$$f_{OAM}(x,y) = f_{odd}(x,y) \pm i f_{even}(x,y), \tag{13}$$

where the $\pm$ sign is determined by the sign of OAM order. The odd and even parts of this equation can be further represented as symmetric or anti-symmetric field functions (f_S or f_A) in X or Y directions, as[24]:

$$f_{odd}(x,y) = f_S(x)f_A(y) \pm i f_A(x)f_S(y), \tag{14}$$

$$f_{even}(x,y) = f_A(x)f_A(y) \pm i f_S(x)f_S(y). \tag{15}$$

Substituting these functions in Eq. (6) and consideration of obtaining one image at the center of a square cross sectional 2D MMI waveguide, the output field profiles at length $3L_c/2K$ can be written as:

$$\Psi_{odd}(x,y,L) = f_S(x)f_A(y)e^{j(\Theta_S(x)\Theta_A(y))} \pm i f_A(x)f_S(y)e^{j(\Theta_A(x)\Theta_S(y))}, \tag{16}$$

$$\Psi_{even}(x,y,L) = f_A(x)f_A(y)e^{j(\Theta_A(x)\Theta_A(y))} \pm i f_S(x)f_S(y)e^{j(\Theta_S(x)\Theta_S(y))}, \tag{17}$$

where Θ_S and Θ_A are the symmetric and anti-symmetric phase terms, respectively, as[48]:

$$\Theta_S(x) = \Theta_S(y) = \left(\frac{K^2}{2K} + \frac{1}{4}\right)\pi, \tag{18}$$
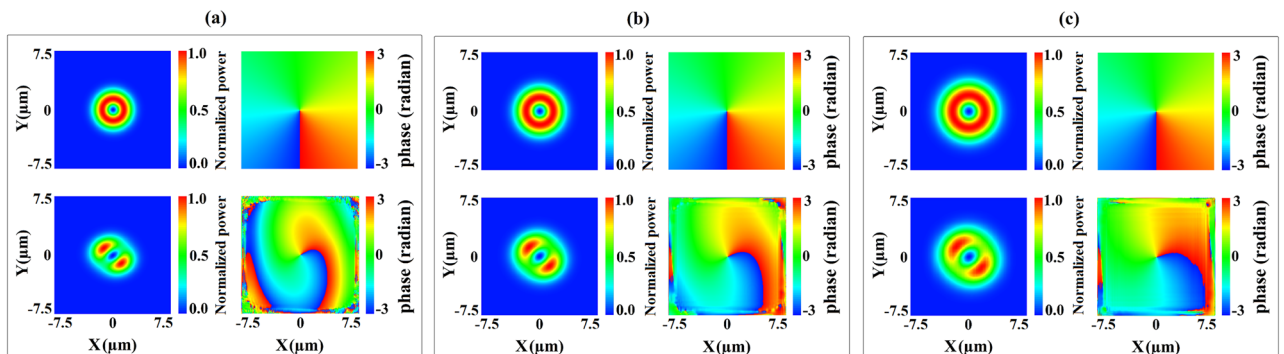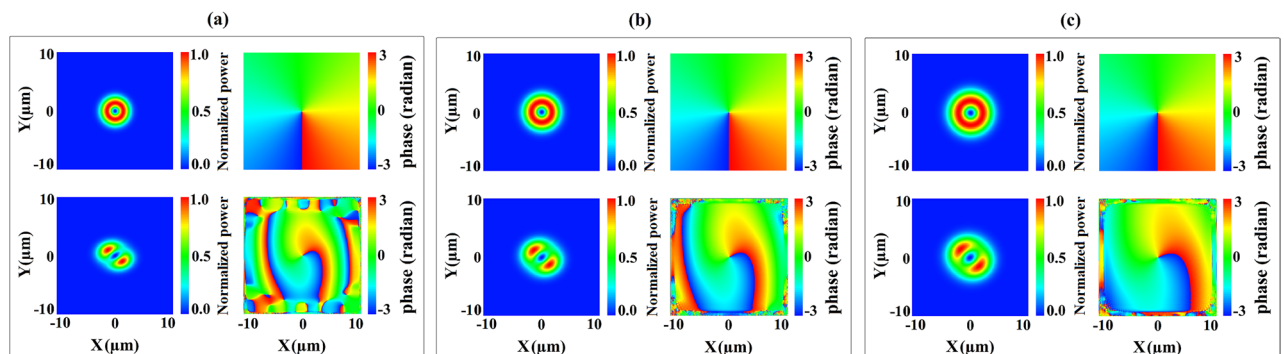

Fig. 2. Normalized power distributions (left) and phase patterns (right) of the input (top rows) first order OAM modes with WR = 2 μm (**a**), WR = 2.5 μm (**b**), and WR = 3 μm (**c**), and output (bottom rows) generated self-images for an MMI waveguide with 15 μm width.

Fig. 3. Normalized power distributions (left) and phase patterns (right) of the input (top rows) first order OAM modes with WR = 2 μm (**a**), WR = 2.5 μm (**b**), and WR = 3 μm (**c**), and output (bottom rows) generated self-images for an MMI waveguide with 20 μm width.

$$\Theta_A(x) = \Theta_A(y) = \left(\frac{K^2}{2K} - \frac{1}{4} \right) \pi. \tag{19}$$

Substituting $K = 1$, which corresponds to $3L_c/2$, the phase terms become:

$$\Theta_S(x) = \Theta_S(y) = \frac{3\pi}{4}, \tag{20}$$

$$\Theta_A(x) = \Theta_A(y) = \frac{\pi}{4}. \tag{21}$$

Hence, the output fields Ψ_{odd} and Ψ_{even} are given as:

$$\Psi_{odd}(x, y, L) = e^{j\pi} \left(f_S(x)f_A(y) \pm if_A(x)f_S(y) \right), \tag{22}$$

$$\Psi_{even}(x, y, L) = e^{\frac{j\pi}{2}} \left(f_A(x)f_A(y) \mp if_S(x)f_S(y) \right). \tag{23}$$

The comparison between Eqs. (22) and (16) as well as 23 and 17 clearly imply that the topological charge of odd order OAM modes remains unchanged after passing through the length $3L_c/2$ of the MMI waveguide, whereas the charge of even order modes is reversed. Therefore, it can be inferred that an MMI waveguide with the length $3L_c/2$ acts as inherent charge converter for OAM modes with even values of ℓ. This fact is schematically shown in Fig. 4.

The performance analysis of produced OAM-maintaining image has already been reported in Table 2 for $\ell = \pm 1$. For higher odd OAM modes, the POI graphs are illustrated in Fig. 5 for input modes with $\ell = \pm 1$ to ± 9 with WR = 3 µm. The graphs show that the higher the OAM mode order, the lower the calculated POI, especially for wider waveguides. However, the wider waveguides can counteract this decrease in POI by increasing the input mode's WR, as explained in the *WR* section.

For even order OAM modes, in order to declare the mentioned mode conversion property, the simulation results for the second, fourth and sixth order of OAM modes propagating along a 20 µm width MMI waveguide
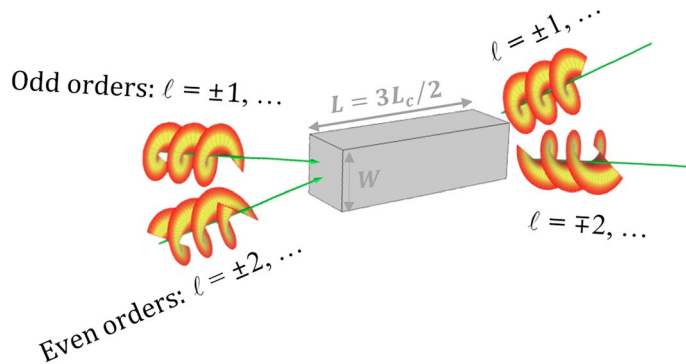

Fig. 4. Schematic diagram of a square cross-sectional 2D MMI waveguide with the length $3L_c/2$. The waveguide acts as a charge converter for OAM modes with even values of ℓ.
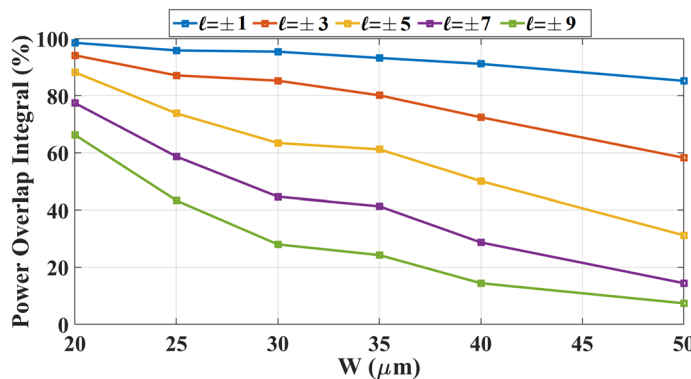

Fig. 5. The calculated POI between the input OAM modes of $\ell = \pm 1$ to ± 9 with WR = 3 µm and their corresponding output generated images.

are shown in Fig. 6. In this figure, left and right columns display the normalized power distributions and phase patterns of the input (top rows) OAM modes of $\ell = +2$ (a), $\ell = +4$ (b), and $\ell = +6$ (c), and the output (bottom rows) generated images of $\ell = -2$ (a), $\ell = -4$ (b), and $\ell = -6$ (c). Comparing the phase patterns of the input modes and the generated images, that are respectively clockwise and counterclockwise for each twist, it is clear that the topological charges are reversed.

In order to find out how well a 2D MMI waveguide can work as a charge converter for even order of OAM modes, the purity of the generated images, E (ρ, θ), are calculated using[49]:

$$Purity = \frac{\int_0^\infty \left| \int_0^{2\pi} E(\rho,\theta)\frac{e^{-il\theta}}{\sqrt{2\pi}}d\theta \right|^2 \rho d\rho}{\int_0^\infty \int_0^{2\pi} |E(\rho,\theta)|^2 d\theta \rho d\rho}. \tag{24}$$

The calculated purity for the mentioned waveguide in Fig. 6 with W = 20 μm is reported in Table 3.

Additionally, in order to illustrate the effect of dimensional variations, the fabrication errors of ± 0.5 μm are introduced into the geometrical parameters of this waveguide. Figure 7 shows the simulation results. For all the three input OAM modes, fabrication errors in the width of MMI waveguide (W_{MMI}) degrade the calculated purity. However, MMI waveguide's length (L_{MMI}) remains essentially flat over the same error range. Consequently, the fabrication tolerance analysis will be concerned only with variations in W_{MMI}, with errors in L_{MMI} assumed to be negligible.

In addition to the dimensional variations, surface roughness is another source of error in waveguides. Sidewall roughness effect in multimode rectangular optical waveguides has been already investigated in some references[52–56]. The theory behind this effect for 2D MMI waveguides can be summarized as follows[53,55].

In a real waveguide, there is irregular distribution at the core-cladding interface, which can be characterized by the roughness σ. It is usually assumed that the distortion function of the core boundary is a stationary random process described by the function $f(z)$.

Assuming x-polarized E_{mn} modes in a rectangular waveguide, the coupling coefficients between the guided modes and the radiation modes caused by the aforementioned waveguide irregularities can be expressed as:

$$K_{mn,\rho} = \frac{\omega\varepsilon_0}{4iP} \int\limits_{-\infty}^{\infty}\int (n^2 - n_0^2)\vec{E}_{mn}^{*(x)}\vec{E}_\rho^{(x)}dxdy \tag{25}$$

where ω is the angular frequency of light, ε_0 is the dielectric constant of vacuum, P is the power factor, $\vec{E}_{mn}^{(x)}$ and $\vec{E}_\rho^{(x)}$ are the electric fields of E_{mn} modes and the radiation modes along the x direction, respectively. The function $n_0(x, y)$ describes the refractive index distribution of the unperturbed waveguide whereas $n(x, y, z)$ specifies the refractive index dependence of the real, distorted waveguide. The scattering loss coefficient α_{mn} of E_{mn} mode induced by σ is a characteristic parameter to describe the influence on the transmission loss of rectangular optical waveguides. According to the standard perturbation theory, α_{mn} can be expressed as:

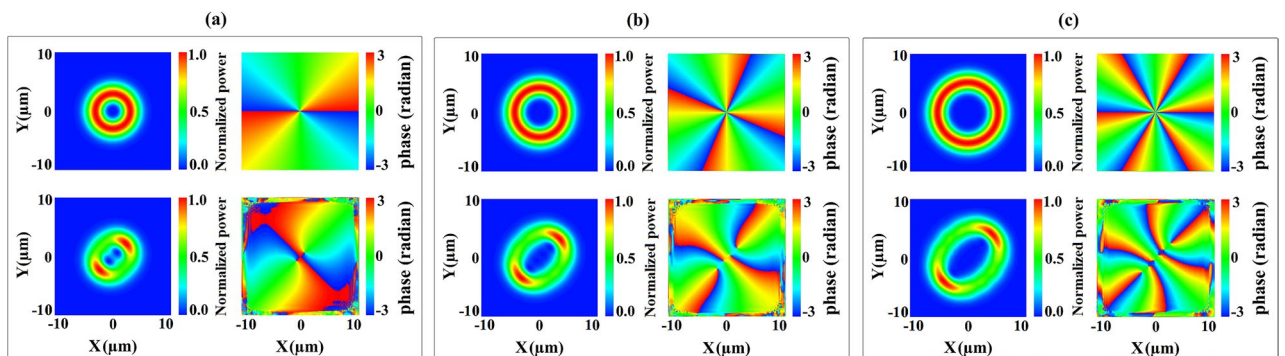**(a)**   **(b)**   **(c)**

Fig. 6. Normalized power distributions (left) and phase patterns (right) of the input (top rows) OAM modes of $\ell = +2$ (**a**), $\ell = +4$ (**b**), and $\ell = +6$ (**c**), and output (bottom rows) generated images of $\ell = -2$ (**a**), $\ell = -4$ (**b**), and $\ell = -6$ (**c**) for an MMI waveguide with 20 μm width. A comparison between the phase pattern of the input modes and the generated images that are respectively clockwise and counterclockwise for each twist, clearly implies that the topological charges are reversed.

Topological charge	Purity (%)
± 2	96.13
± 4	84.85
± 6	82.03

Table 3. The calculated purity for the mentioned waveguide in Fig. 6.

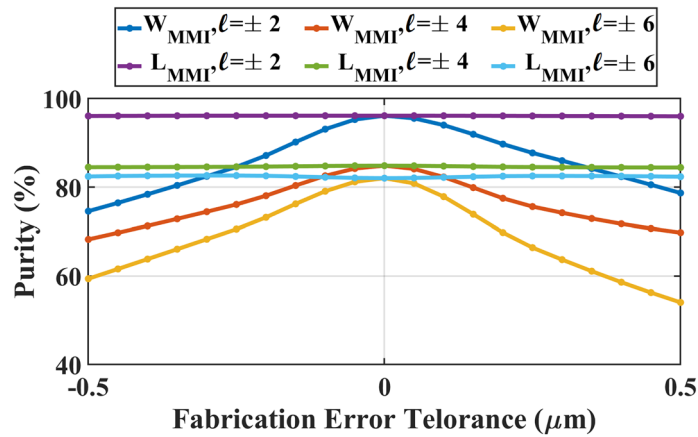**Fig. 7.** The effects of the fabrication errors on the calculated Purity; when a deviation of ± 0.5 μm is applied into the width and length of the mentioned waveguide in Fig. 6. The fabrication errors in W_{MMI} degrades the calculated purity. However, L_{MMI} remains essentially flat over the same error range.

$$\alpha_{mn} = \iint \sum_{s=1}^{4} \left| K_{mn,\rho}^{s}(\kappa, \nu) \right|^2 \langle \left| F^s\left(\beta_{mn} - \beta_\rho\right) \right|^2 \rangle d\kappa\, d\nu \qquad (26)$$

The different coupling coefficients $K_{mn,\rho}^s(\kappa, \nu)$ are assigned to the different sidewalls s of the waveguide. The distortion is introduced by the Fourier transform of the autocorrelation function of the stochastic distortion process:

$$\langle \left| F^s\left(\beta_{mn} - \beta_\rho\right) \right|^2 \rangle = \int_{-\infty}^{\infty} \langle f^{(s)}(z) f^{(s)}(z-u) \rangle exp\left[-i\left(\beta_{mn} - \beta_\rho\right) u \right] du \qquad (27)$$

In order to determine the scattering loss coefficient α_{mn} induced by the roughness σ, calculation of coupling coefficients $K_{mn,\rho}^s(\kappa, \nu)$ using efficient analytical methods is necessary. Finite-difference time domain (FDTD)[57] and ray tracing[58] have been used for this propose. Furthermore, a precise analytical method, the radiation-mode Fourier decomposition method (RFDM) has been introduced[56]. As seen in Eq. 26, regardless of what is the incident field into the waveguide, the analysis of roughness effect is performed by calculating coupling coefficients between guided and radiated modes of the waveguide. On the other hand, as mentioned, these calculations need applying analytical methods, which are elaborative and time-consuming process. Therefore, to maintain the continuity of this paper, which focuses on the behavior of OAM modes in 2D rectangular MMI waveguides (not just the 2D MMI waveguides features per se), and also to avoid content overload, performing the analytical solution is omitted.

Conclusion

This paper presents a study on OAM modes propagation in 2D square cross-sectional MMI waveguides, which leads to be known the mode conversion property of these waveguides. Based on OAM-MMI theory, OAM modes form an OAM-maintaining image at distance $3L_c/2$ of an MMI waveguide, where, L_c is the coupling length between the two lowest order modes. In order to investigate the potential of MMI waveguides at this length for OAM integrated applications, the properties of generated images are studied by considering the effects of three parameters including the width of the waveguide, WR of the OAM mode and its topological charge. It is mathematically shown that the topological charge of odd order OAM modes remains unchanged at OAM-maintaining length, whereas the charge of even order modes is reversed. In other words, an MMI waveguide with the length $3L_c/2$ acts as a charge converter for OAM modes with even values of ℓ. To numerically confirm this fact, the simulations are performed using BPM method for silicon waveguides surrounded by silica which are compatible with silicon on insulator (SOI) technology. The waveguides are assumed to have width of 15–50 μm, at the working wavelength of 1550 nm. The quality of the generated modes is evaluated by calculation of POI and the purity for input OAM modes with WR in a range of 1.5–3.5 μm. The results demonstrate that the calculated POI is enhanced by increasing in WR of the input mode. However, for a specific WR value, the increase in the waveguide's width leads to decrease the quality of the self-imaged mode. Therefore, choosing the right size for MMI waveguides to achieve a desired mode quality requires an appropriate input mode's WR selection. According to the results of this study, 2D cross-sectional MMI waveguides at their OAM-maintaining length can be used in a wide range of integrated OAM applications as the integrated OAM waveguides, mode convertors, switches, and couplers.

Data availability

Data supporting this study are available from the corresponding author on reasonable request.

References

1. Allen, L., Beijersbergen, M. W., Spreeuw, R. & Woerdman, J. Orbital angular momentum of light and the transformation of Laguerre–Gaussian laser modes. *Phys. Rev. A* **45**, 8185 (1992).
2. Liu, J., Li, S., Zhu, L. & Wang, J. In *Asia Communications and Photonics Conference.* ASu2A. 101 (Optica Publishing Group).
3. Wang, J. *et al.* Terabit free-space data transmission employing orbital angular momentum multiplexing. *Nat. Photonics* **6**, 488–496 (2012).
4. Willner, M. J. *et al.* In *2013 IEEE Photonics Conference* 1–2 (IEEE).
5. Longman, A. & Fedosejevs, R. Mode conversion efficiency to Laguerre-Gaussian OAM modes using spiral phase optics. *Opt. Express* **25**, 17382–17392 (2017).
6. Gregg, P. *et al.* In *2015 Conference on Lasers and Electro-Optics (CLEO)* 1–2 (IEEE).
7. Yan, L. *et al.* Q-plate enabled spectrally diverse orbital-angular-momentum conversion for stimulated emission depletion microscopy. *Optica* **2**, 900–903 (2015).
8. Mirhosseini, M. *et al.* Rapid generation of light beams carrying orbital angular momentum. *Opt. Express* **21**, 30196–30203 (2013).
9. Zhou, J., Zhang, W. & Chen, L. Experimental detection of high-order or fractional orbital angular momentum of light based on a robust mode converter. *Appl. Phys. Lett.* **108**, 111108 (2016).
10. Pan, J. *et al.* Index-tunable structured-light beams from a laser with an intracavity astigmatic mode converter. *Phys. Rev. Appl.* **14**, 044048 (2020).
11. Carpenter, J., Thomsen, B. C. & Wilkinson, T. D. In *Optical Fiber Communication Conference.* OTh4G. 3 (Optica Publishing Group).
12. Zhao, Y. *et al.* Mode converter based on the long-period fiber gratings written in the two-mode fiber. *Opt. Express* **24**, 6186–6195 (2016).
13. Zhao, H. *et al.* Broadband flat-top second-order OAM mode converter based on a phase-modulated helical long-period fiber grating. *Opt. Express* **29**, 29518–29526 (2021).
14. Zhu, C. *et al.* On-demand flat-top wideband OAM mode converter based on a cladding-etched helical fiber grating. *Opt. Express* **31**, 43477–43489 (2023).
15. Zhao, X., Liu, Y., Liu, Z. & Mou, C. All-fiber bandwidth tunable ultra-broadband mode converters based on long-period fiber gratings and helical long-period gratings. *Opt. Express* **28**, 11990–12000 (2020).
16. Mansuripur, M., Zakharian, A. R. & Wright, E. M. Spin and orbital angular momenta of light reflected from a cone. *Phys. Rev. A At. Mol. Opt. Phys.* **84**, 033813 (2011).
17. Thalhammer, G., Bowman, R. W., Love, G. D., Padgett, M. J. & Ritsch-Marte, M. Speeding up liquid crystal SLMs using overdrive with phase change reduction. *Opt. Express* **21**, 1779–1797 (2013).
18. Cai, X. *et al.* Integrated compact optical vortex beam emitters. *Science* **338**, 363–366 (2012).
19. Fatkhiev, D. M. *et al.* Recent advances in generation and detection of orbital angular momentum optical beams—A review. *Sensors* **21**, 4988 (2021).
20. Zhang, N. *et al.* Large-scale integrated reconfigurable orbital angular momentum mode multiplexer. arXiv preprint arXiv:2008.00680 (2020).
21. Zhu, J., Cai, X., Chen, Y. & Yu, S. Theoretical model for angular grating-based integrated optical vortex beam emitters. *Opt. Lett.* **38**, 1343–1345 (2013).
22. Chen, Y., Lin, Z., Belanger-de Villers, S., Rusch, L. A. & Shi, W. WDM-compatible polarization-diverse OAM generator and multiplexer in silicon photonics. *IEEE J. Sel. Top. Quantum Electron.* **26**, 1–7 (2019).
23. Su, T. *et al.* Demonstration of free space coherent optical communication using integrated silicon photonic orbital angular momentum devices. *Opt. Express* **20**, 9396–9402 (2012).
24. Sun, J., Moresco, M., Leake, G., Coolbaugh, D. & Watts, M. R. Generating and identifying optical orbital angular momentum with silicon photonic circuits. *Opt. Lett.* **39**, 5977–5980 (2014).
25. Liu, A. *et al.* On-chip generation of the reconfigurable orbital angular momentum with high order. *Opt. Express* **28**, 17957–17965 (2020).
26. Xie, Z. *et al.* Ultra-broadband on-chip twisted light emitter for optical communications. *Light Sci. Appl.* **7**, 18001–18001 (2018).
27. Zhou, N. *et al.* Ultra-compact broadband polarization diversity orbital angular momentum generator with 3.6 × 3.6 μm² footprint. *Sci. Adv.* **5**, eaau9593 (2019).
28. Willner, A. E., Su, X., Song, H., Zhou, H. & Zou, K. Integrated circuits based on broadband pixel-array metasurfaces for generating data-carrying optical and THz orbital angular momentum beams. *Nanophotonics* **12**, 2669 (2023).
29. Lyubopytov, V. S., Kutluyarov, R. V., Bagmanov, V. K., Neumann, N. & Sultanov, A. K. Modeling and optimization of vortex modes propagation in rectangular dielectric waveguides. *IEEE Photonics J.* **12**, 1–17 (2019).
30. Zhang, D., Feng, X., Cui, K., Liu, F. & Huang, Y. Generating in-plane optical orbital angular momentum beams with silicon waveguides. *IEEE Photonics J.* **5**, 2201206–2201206 (2013).
31. Li, W., Liu, J., Gao, Y., Zhou, K. & Liu, S. Dynamics of angular momentum-torque conversion in silicon waveguides. *Opt. Express* **27**, 10208–10220 (2019).
32. Mousavi, S. F., Vallone, G., Villoresi, P. & Nouroozi, R. Generation of mutually unbiased bases for 4D-QKD with structured photons via LNOI photonic wire. *J. Opt.* **20**, 095802 (2018).
33. Zheng, S. & Wang, J. On-chip orbital angular momentum modes generator and (de) multiplexer based on trench silicon waveguides. *Opt. Express* **25**, 18492–18501 (2017).
34. Liang, Y., Wu, H. W., Huang, B. J. & Huang, X. G. Light beams with selective angular momentum generated by hybrid plasmonic waveguides. *Nanoscale* **6**, 12360–12365 (2014).
35. Liang, Y., Zhang, F., Gu, J., Huang, X. G. & Liu, S. Integratable quarter-wave plates enable one-way angular momentum conversion. *Sci. Rep.* **6**, 24959 (2016).
36. Ni, F. C., Xie, Z. T., Hu, X.-D., Jia, C.-Y. & Huang, X. G. Selective angular momentum generator based on a graphene hybrid plasmonic waveguide. *J. Lightwave Technol.* **37**, 5486–5492 (2019).
37. Zhang, D. Angular momentum of optical modes in a silicon channel waveguide. *Phys. Rev. Res.* **2**, 033454 (2020).
38. Fatkhiev, D. M., Lyubopytov, V. S., Kutluyarov, R. V., Grakhova, E. P. & Sultanov, A. K. A grating coupler design for optical vortex mode generation in rectangular waveguides. *IEEE Photonics J.* **13**, 1–8 (2021).
39. Soldano, L. B. & Pennings, E. C. Optical multi-mode interference devices based on self-imaging: Principles and applications. *J. Lightwave Technol.* **13**, 615–627 (1995).
40. Chack, D., Hassan, S. & Kumar, A. In *Integrated Optics: Devices, Materials, and Technologies XXIV* 238–243 (SPIE).
41. Jiao, Y., Dai, D., Shi, Y. & He, S. Shortened polarization beam splitters with two cascaded multimode interference sections. *IEEE Photonics Technol. Lett.* **21**, 1538–1540 (2009).
42. Yao, Y., Wang, W. & Zhang, B. Designing MMI structured beam-splitter in LiNbO₃ crystal based on a combination of ion implantation and femtosecond laser ablation. *Opt. Express* **26**, 19648–19656 (2018).

43. Wageeh, A., El-Sabban, S. & Khalil, D. Design of a 2D fiber mode converter using a planar 2D multi-mode interference structure. *Optik* **210**, 164500 (2020).
44. Nuck, M. *et al.* In *Integrated Optics: Devices, Materials, and Technologies XXIII* 163–171 (SPIE).
45. Zhou, Y. Silicon-based mode converter and demultiplexer for wavelength division multiplexing transmission by using multimode interference couplers. *Opt. Photonics J.* **10**, 117 (2020).
46. Linh, H. D. T., Truong, D. C., Quang, D. D., Phuc, V. D. & Hung, N. T. In *2019 6th NAFOSTED Conference on Information and Computer Science (NICS)* 98–102 (IEEE).
47. Jiang, X., Sun, Y., Yang, J. & Wang, M. General imaging properties of two-dimensional multimode interference couplers. *Opt. Eng.* **45**, 044602–044602–044607 (2006).
48. Ma, Z. *et al.* Self-imaging of orbital angular momentum (OAM) modes in rectangular multimode interference waveguides. *Opt. Express* **23**, 5014–5026 (2015).
49. Soltani, A., Firouzeh, Z. H., Mousavi, S. F., Nezhad, A. Z. & Nouroozi, R. Mode conversion between beams carrying orbital angular momentum with opposite topological charges using two-dimensional multimode interference waveguides. *J. Lightwave Technol.* **41**, 2179–2184 (2022).
50. Jiang, X., Mao, H. & Wang, M. In *Optical Fiber and Planar Waveguide Technology II* 51–56 (SPIE).
51. Khalil, D. & Yehia, A. Two-dimensional multimode interference in integrated optical structures. *J. Opt. A Pure Appl. Opt.* **6**, 137 (2003).
52. Barwicz, T. & Haus, H. A. Three-dimensional analysis of scattering losses due to sidewall roughness in microphotonic waveguides. *J. Lightwave Technol.* **23**, 2719 (2005).
53. Deng, C. *et al.* Roughness estimation of multimode rectangular optical waveguide based on the scattering loss difference between SMFW and MMFW structures. *IEEE Photonics J.* **9**, 1–13 (2017).
54. Di Donato, A. *et al.* Stationary mode distribution and sidewall roughness effects in overmoded optical waveguides. *J. Lightwave Technol.* **28**, 1510–1520 (2010).
55. Lenz, D., Erni, D. & Bächtold, W. Modal power loss coefficients for highly overmoded rectangular dielectric waveguides based on free space modes. *Opt. Express* **12**, 1150–1156 (2004).
56. Papakonstantinou, I., James, R. & Selviah, D. R. Radiation-and bound-mode propagation in rectangular, multimode dielectric, channel waveguides with sidewall roughness. *J. Lightwave Technol.* **27**, 4151–4163 (2009).
57. Poulton, C. G. *et al.* Radiation modes and roughness loss in high index-contrast waveguides. *IEEE J. Sel. Top. Quantum Electron.* **12**, 1306–1321 (2006).
58. Bierhoff, T., Wallrabenstein, A., Himmler, A., Griese, E. & Mrozynski, G. Ray tracing technique and its verification for the analysis of highly multimode optical waveguides with rough surfaces. *IEEE Trans. Magn.* **37**, 3307–3310 (2001).

Author contributions

A.S., R.N., and Z.H. conceived the idea. A.S. carried out the theoretical analysis, simulation and writing the manuscript. All authors reviewed the manuscript and discussed the results.

Competing interests

The authors declare no competing interests.

Additional information

Correspondence and requests for materials should be addressed to Z.H.F.

Reprints and permissions information is available at www.nature.com/reprints.

Publisher's note Springer Nature remains neutral with regard to jurisdictional claims in published maps and institutional affiliations.